Mathematical Biosciences and Engineering

http://www.aimspress.com/journal/MBE

MBE, 23(3): 678–701.
DOI: 10.3934/mbe.2026026
Received: 11 August 2025
Revised: 18 December 2025
Accepted: 04 January 2026
Published: 28 January 2026

Research article

Digital twin for ocular hemodynamics: Combining physiology-based modeling and machine learning for personalized glaucoma care

Giovanna Guidoboni[1,2,*], James M. Keller[3], Christopher K. Wikle[4], Rajat Rai[2], Mikey Joyce[3], Omar Ibrahim[5], Daphne Zou[3], Rachel S. Chong[6,7], Ching-Yu Cheng[6,8,9], Brent A. Siesky[10], Alice C. Verticchio Vercellin[10], Keren Wood[10] and Alon Harris[3,10]

[1] Maine College of Engineering and Computing, University of Maine, ME, USA
[2] Graduate School of Biomedical Science and Engineering, University of Maine, ME, USA
[3] Department of Electrical Engineering and Computer Science, University of Missouri, MO, USA
[4] Department of Statistics, University of Missouri, MO, USA
[5] Department of Electrical Engineering, Tikrit University, Tikrit, Iraq
[6] Singapore Eye Research Institute, Singapore, Singapore
[7] Duke-NUS Graduate Medical School, Singapore, Singapore
[8] National University of Singapore, Singapore, Singapore
[9] Center for Innovation and Precision Eye Health, Yong Loo Lin School of Medicine, National University of Singapore, Singapore, Singapore
[10] Department of Ophthalmology, Icahn School of Medicine at Mount Sinai Hospital, NY, USA

* **Correspondence:** Email: giovanna.guidoboni@maine.edu; Tel: +1-207-581-2217; Fax: +1-207-581-2220.

Abstract: This work investigated the combined effects of intraocular pressure (IOP) and blood pressure (BP) on retinal hemodynamics and glaucoma progression using a novel, physiology-based digital twin for ocular hemodynamics (DT-OH). The DT-OH integrates a mathematical model of ocular physiology with machine learning to simulate retinal blood flow dynamics based on individualized IOP and BP inputs. The DT-OH was applied to clinical data from the Indianapolis Glaucoma Progression Study (IGPS) to characterize how IOP and BP jointly influence retinal hemodynamics and their association with glaucoma progression. The DT-OH identified three distinct hemodynamic profiles based on the combined effects of IOP and BP. Membership in one specific profile at baseline was associated with a significantly higher risk of glaucoma progression. These profiles reflect distinct patterns of ocular blood flow regulation and provide physiological insight into the interplay between systemic and ocular factors in glaucoma. These findings enhance our understanding of glaucoma pathophysiology and support the development of personalized risk assessment tools that account for both IOP and BP.

Keywords: digital twin; mathematical modeling; machine learning; glaucoma; hemodynamics

1. Introduction

Glaucoma is a multi-factorial disease characterized by progressive optic nerve damage and irreversible vision loss. Historically, glaucoma has been associated with elevated intraocular pressure (IOP); however, many patients develop and experience disease and its progression despite low or therapeutically lowered IOP [1]. Non-IOP risk factors include advancing age, myopia, both high and low blood pressure (BP), and dysregulated ocular blood flow [2–6].

As the significance of ocular hemodynamics continues to be demonstrated in glaucoma [7], the impact of BP on blood flow and subsequent disease progression is likely extremely high. However, translating and predicting disease onset and progression from factors other than IOP, including BP and ocular blood flow, remains an urgent unmet challenge. Multiple clinical and population-based studies have attempted to shed light on the relationship between IOP, BP, ocular blood flow, and glaucoma. However results are conflicting, with some pointing to low BP [8–10] and others to high BP [11–13] and BP variability [14–17] as increasing risk. The enigma of contributing mechanism(s) linking IOP, BP, and glaucoma remains a major hurdle for developing new management strategies aimed at co-regulating IOP, BP, and blood flow [2, 18].

In recent years, digital twins have emerged as useful tools to understand the behavior of complex

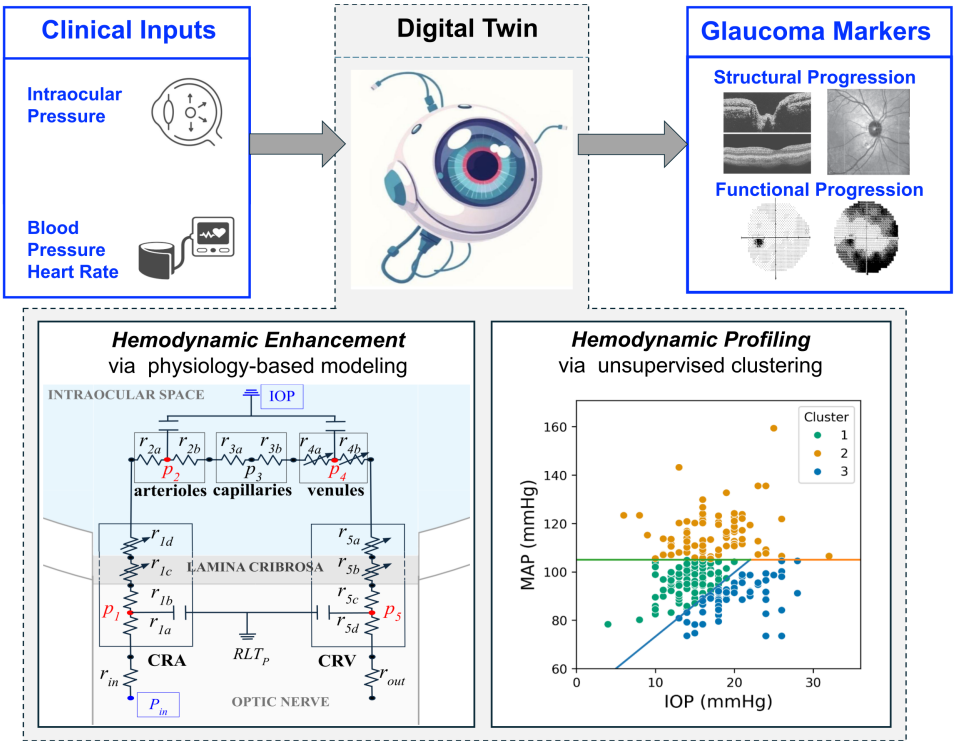

Figure 1. Schematic of the digital twin for ocular hemodynamics (DT-OH) and its application for a personalized prediction of glaucoma progression.

systems, especially when intervening on the physical systems may be too costly, time-intensive, or infeasible [19–21]. Stemming from mechanism-driven modeling and propelled by the rapid advancements in machine learning (ML) and artificial intelligence (AI), digital twins are rapidly unlocking new possibilities for understanding the human body [22]. Recent work in computational modeling and digital twin systems in biomedical engineering has further validated their utility for predictive, personalized healthcare applications [23, 24]. While cardiology and oncology remain at the forefront of digital twin applications, their potential in ophthalmology is beginning to emerge [25].

This work develops a new digital twin approach, named the digital twin for ocular hemodynamics (DT-OH), to aid the study and management of glaucoma. The DT-OH is an integrated personalized digital twin that combines a physiology-based mathematical model of retinal circulation with an unsupervised clustering pipeline to produce individualized hemodynamic biomarkers and assign hemodynamic phenotypes to generate personalized risk profiles for glaucoma progression. The workflow is a multi-step process as schematized in Figure 1: A subset of easily accessible measurements (IOP, BP, HR) is used as individualized inputs for a physiology-based mathematical model of the retinal circulation [26, 31] that provides enhanced features quantifying the impact of the individual-specific IOP and BP values on ocular hemodynamics (Section 2.2). Next, unsupervised clustering methods from machine learning are used for hemodynamic profiling, namely to identify the eye group that is hemodynamically similar to the one under consideration (Section 2.3). Individualized risk of glaucoma progression is then evaluated by investigating structural and functional markers on the basis of the DT-OH-enabled individualized profiling (Section 2.4).

When applied to a longitudinal clinical study on glaucoma eyes (Section 2.1), the Indianapolis Glaucoma Progression Study [27], the DT-OH approach successfully identified three clusters of hemodynamically similar eyes based on their IOP and BP baseline values. Importantly, belonging to one specific cluster was indicative of reduced risk for glaucoma progression based on retinal nerve fiber layer thickness, cup-to-disc ratio, and visual field mean deviation (Section 3.4). The DT-OH profiling enables us to formulate hypotheses on the potential mechanisms underlying glaucoma risk, which may be driven by limited regulation capacity or elevated venous compression depending on the eye-specific IOP-BP combinations.

2. Materials and methods

The DT-OH approach developed in this work is based on two main components, namely:

1. *a physiology-based mathematical model* that takes eye-specific inputs to generate enhanced hemodynamic features quantifying eye-specific impact of IOP and BP values measured clinically (Section 2.2);
2. *an unsupervised machine learning and clustering* analysis that profiles the eyes on the grounds of their similarities in terms of the enhanced feature set (Section 2.3).

The DT-OH is applied to data from the Indianapolis Glaucoma Progression Study (Section 2.1), and the outcomes are analyzed using glaucoma markers characterizing progression in terms of structural and functional changes in the eye (Section 2.4).

2.1. Clinical dataset

The dataset utilized here comes from the Indianapolis Glaucoma Progression Study (IGPS), an observational study comprising 114 eyes (70 females, 44 males) diagnosed with open angle glaucoma (OAG). Throughout the study, assessments of patients were conducted every 6 months over a span of several years. We remark that the evaluations are based on one eye per patient. The IGPS dataset contains values of IOP, systolic BP (SBP), diastolic BP (DBP) and HR, along with the following clinical OAG markers: (i) horizontal and vertical cup-to-disc (C/D) ratios defined as the ratios between corresponding cup and disc diameters (Figure 2(a), and retinal nerve fiber layer (RNFL) thickness, measured through Stratus (Zeiss, Meditec, Dublin, CA) optical coherence tomography (OCT). For this study, we specifically consider the average RNFL thickness, defined as the mean thickness across all circumpapillary sectors (temporal, superior, nasal, and inferior) around the optic nerve head, as illustrated in Figure 2(b); (ii) mean deviation (MD) and pattern standard deviation (PSD), obtained via visual field testing; and (iii) blood velocities in the central retinal artery and ophthalmic artery obtained via color doppler imaging (CDI), a noninvasive ultrasound technique used to assess ocular blood flow. Specifically, the derived CDI markers include peak-systolic velocity, end-diastolic velocity, and resistivity index in the ophthalmic artery (OAsys, OAdys, OAri) and the central retinal artery (CRAsys, CRAdys, CRAri) [2, 30]. In the IGPS, the data collection was performed by the same two operators throughout the duration of the study, including all follow-up visits. All visits for the same patient were scheduled approximately at the same time of the day.

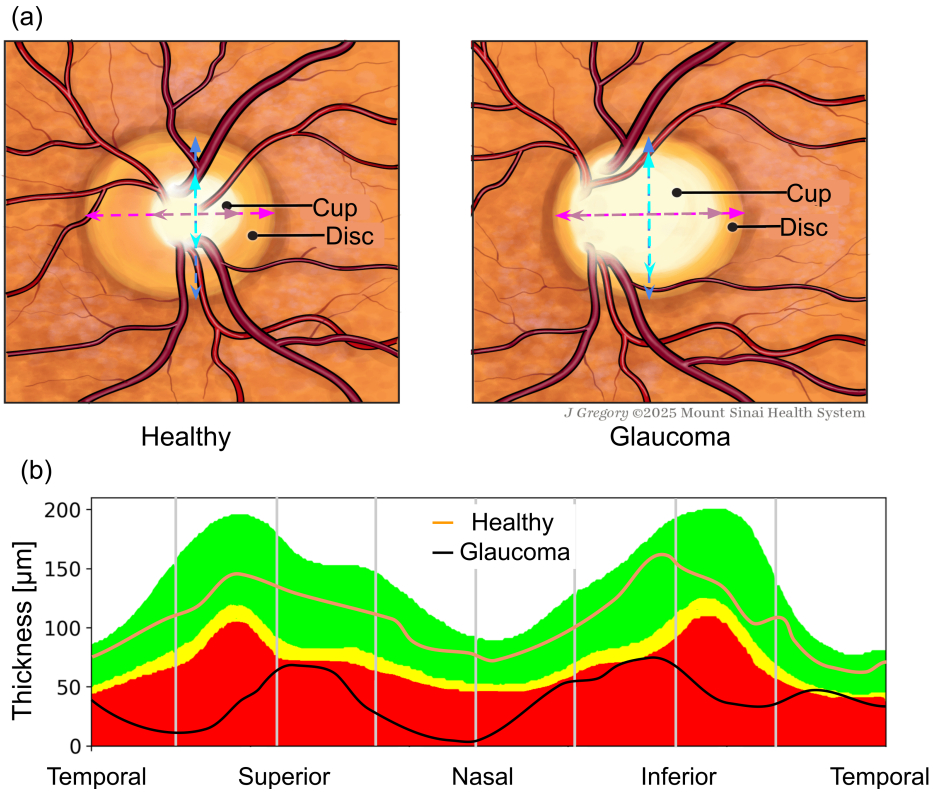

Figure 2. (a) Illustrative optic nerve head images: vertical C/D ratio (blue lines), courtesy of *Ms. Jill Gregory*; horizontal C/D ratio (magenta lines); (b) illustrative OCT RNFL profiles from a standard circumpapillary scan around the optic nerve head.

2.2. *Physiology-based mathematical model*

The first component of the DT-OH involves a previously validated mathematical model [26], which is used to obtain physiology-based hemodynamic features of an individual's eye based on clinically measured IOP and BP data. The model consists of a set of nonlinear ordinary differential equations (ODEs) simulating blood flow through the retinal vasculature, as depicted in Figure 3, along with a schematic illustration of the eye for ease of reference. The central retinal artery (CRA) and the central retinal vein (CRV) run parallel to each other in the optic nerve. After passing through the lamina cribrosa, the CRA enters the intraocular space and branches into arterioles, capillaries, and venules, which ultimately converge into the CRV before leaving the eye. The intraocular vessels are exposed to IOP, while the CRA and CRV segments within the optic nerve are exposed to the retrolaminar tissue pressure ($RLT\,p$). The blood flow through the retinal circulation is driven by the pressure difference on the arterial inlet (P_{in}) and the venous outlet (P_{out}).

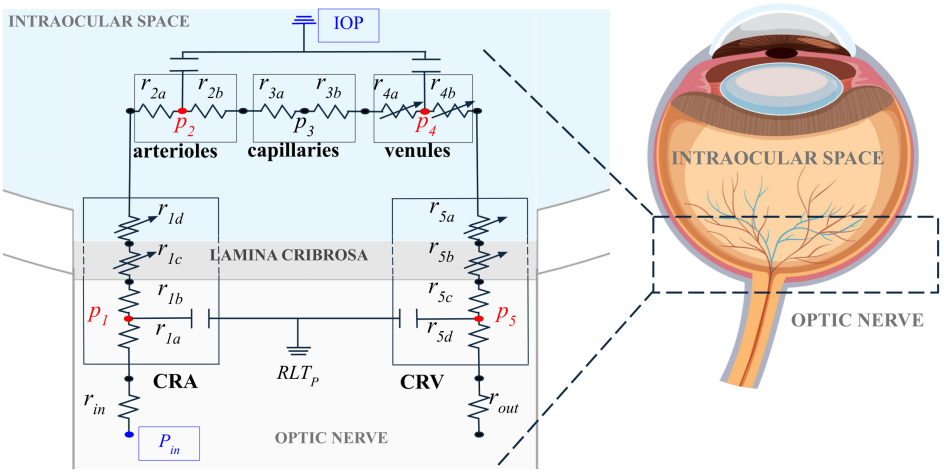

Figure 3. Representation of the physiology-based mathematical model for the retinal circulation based on the electric analogy to fluid flow (left), accompanied by a schematic illustration of the eye (right). Image of eye by *brgfx* on *FreePIK*.

Leveraging the electric analog to fluid flow, the model comprises capacitances and resistances to include the deformability of blood vessels and the viscous effects of blood flow through them. Nonlinear resistances are indicated with an arrow and they capture the IOP-induced blood vessel deformation. We note that here the model is utilized with a constant arteriolar resistance, in order to predict hemodynamic conditions in the absence of autoregulation.

IOP values obtained from clinical measurements are utilized as individualized model input for the pressure in the intraocular space. Furthermore, individualized clinical measurements of SBP, DBP, and HR are used to define P_{in}, following the procedure detailed in Rai et al [31]. All other model parameters are kept at their baseline values reported in the original article [26]. For each set of clinically measured individualized inputs, the nonlinear ODE system provides time-dependent pressures, resistances, and flow rates. The system is solved over a time interval corresponding to 10 cardiac cycles, in order to ensure that a periodic solution is attained. The last simulated cycle is then utilized to compute all quantities of interest, which include averages of the total retinal blood flow (Q), vascular pressures (P), and

Table 1. Physiology-based model inputs and outputs simulating different possible patient conditions. IOP, mean arterial pressure (MAP), P_1, P_2, P_4, P_5 are in [mmHg]; R_4, R_5 are in [10^2 mmHg s ml^{-1}]; Q is in [10^{-4} ml s^{-1}].

IOP	SBP	DBP	MAP	HR	P_1	P_2	P_4	P_5	Q	R_4	R_5
16	90	60	70	80	34	29	19	17	5	58	22
16	120	80	93	80	43	36	22	19	7	51	22
16	130	90	103	80	47	38	23	20	8	48	22
25	90	60	70	80	38	34	27	16	3	121	181
25	120	80	93	80	48	42	31	18	5	51	147
25	130	90	103	80	51	44	32	18	6	47	134

vascular resistances (R). Here we focus on the pressures associated with deformable vascular compartments, namely P_i with $i = 1, 2, 4, 5$, and resistances associated with venous compartments, namely R_4 and R_5. This choice is supported by the leading role that these quantities have in characterizing retinal hemodynamic status, as studied in [31]. Denoting by (t_0, t_{end}) the time interval corresponding to the last cardiac cycle, the averaged pressures are computed as

$$P_i = \frac{1}{t_{end} - t_0} \int_{t_0}^{t_{end}} p_i(t)dt, \quad i = 1, 2, 4, 5, \tag{2.1}$$

whereas the average resistances are computed as

$$R_4 = \frac{1}{t_{end} - t_0} \int_{t_0}^{t_{end}} [r_{4a}(t) + r_{4b}(t)]dt \tag{2.2}$$

$$R_5 = \frac{1}{t_{end} - t_0} \int_{t_0}^{t_{end}} [r_{5a}(t) + r_{5b}(t) + r_{5c} + r_{5d}]dt \tag{2.3}$$

Finally, the average total flow rate is taken to be the mean of the integral averages within different sections of the retinal vasculature, namely:

$$Q = \frac{Q_{12} + Q_{24} + Q_{45}}{3} \tag{2.4}$$

where

$$Q_{12} = \frac{1}{t_{end} - t_0} \int_{t_0}^{t_{end}} \frac{p_1(t) - p_2(t)}{r_{1b} + r_{1c}(t) + r_{1d}(t) + r_{2a}} dt \tag{2.5}$$

$$Q_{24} = \frac{1}{t_{end} - t_0} \int_{t_0}^{t_{end}} \frac{p_2(t) - p_4(t)}{r_{2b} + r_{3a} + r_{3b} + r_{4a}(t)} dt \tag{2.6}$$

$$Q_{45} = \frac{1}{t_{end} - t_0} \int_{t_0}^{t_{end}} \frac{p_4(t) - p_5(t)}{r_{4b}(t) + r_{5a}(t) + r_{5b}(t) + r_{5c}} dt. \tag{2.7}$$

Table 1 reports the value of the model outputs for different combinations of IOP and BP values. As shown, the resulting average pressures, flow, and resistances do not scale linearly with the corresponding inputs. The model exhibits pronounced nonlinear behavior: modest increases in IOP or decreases

in MAP produce reductions in downstream pressures (P_2, P_4, P_5) and disproportionately large changes in the venous resistances R_4 and R_5. For example, at MAP = 70 mmHg, increasing IOP from 16 to 25 mmHg reduces Q from 5×10^{-4} to 3×10^{-4} ml s^{-1} while more than doubling R_4 from 50×10^2 to 121×10^2 mmHg s ml^{-1}. These nonlinear trends are also illustrated in Figure 4.

2.3. *Unsupervised machine learning and clustering*

The second component of the DT-OH focuses on translating the physiology-enhanced hemodynamic representation of each eye obtained in Section 2.2 into phenotypes. To do this, we apply an unsupervised machine learning approach to cluster the eyes based on their individualized representations. These DT-OH-based groupings provide a data-driven way to evaluate whether shared hemodynamic patterns correspond to distinct risks of glaucoma progression, which is assessed *a-posteriori* based on structural and functional markers, as described in Section 2.4.

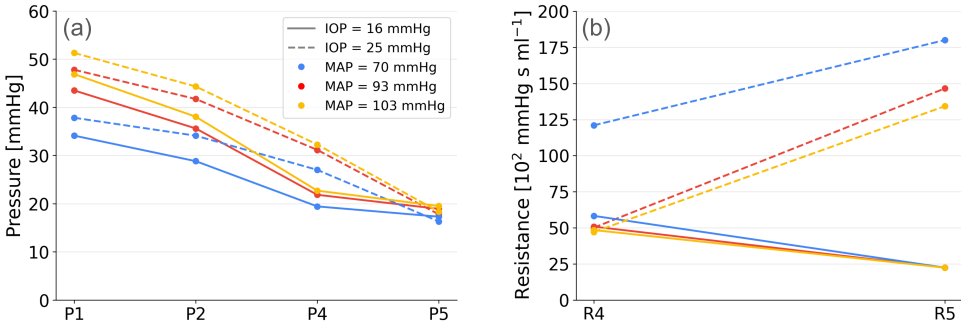

Figure 4. Average pressure and resistance values for different combinations of IOP and MAP throughout different compartments of the physiology-based mathematical model. Notably, lower MAP and higher IOP lead to a stark increase in the venous resistances.

The 7 physiology-enhanced model outputs (Table 2, lower part) are combined with 5 patient-specific clinical data (Table 2, upper part) to define a 12-dimensional (12-D) feature space that is analyzed using unsupervised clustering methods, as described in the next section. We note that the mean arterial pressure (MAP) defined as MAP = (1/3) SBP + (2/3) DBP is included as one of the clinical features even though it is not directly utilized as an input for the physiology-based model. This choice is motivated by the fact that MAP is a quantity of established clinical interest in defining the pressure status of a patient and, consequently, it has been added to the feature space. While the physiology-based enhancement of the initial dataset enriches it by increasing the size of the feature set, the dataset is still quite modest for machine learning. Hence, we require an algorithm that is relatively simple in design and parameters, and yet powerful enough to delineate structure and provide clinical links to glaucoma progression.

We chose the fuzzy C-means (FCM) algorithm based on Euclidean distance and min-max normalization as that approach. The FCM algorithm allows for each point in the dataset to have memberships in all clusters. These memberships are also referred to as "soft memberships" and capture the fact that each point may belong simultaneously to multiple clusters with different degrees of memberships ranging between 0 and 1. When cluster labels are assigned to each data point based on the highest membership value, then we talk about "hard memberships". In the context of glaucoma, this means that each eye will be most similar to those in the cluster for which it has the highest membership. The

same eye will also have some degree of membership in the other clusters, and this provides a quantitative metric to assess how definite the cluster classification is for that eye. This ability of FCM to capture overlapping patterns through soft memberships is particularly suitable for glaucoma datasets, that are often characterized by measurements with intrinsic uncertainty and variability (e.g., BP and IOP measurements) [32, 33].

Table 2. Features comprising the 12-dimensional feature set used for unsupervised clustering. The feature set includes five clinical measurements and seven physiology-enhanced hemodynamic outputs generated by the physiology-based mathematical model that constitutes the first component of the DT-OH framework.

Type	Symbol	Quantity
Clinical Data	IOP	Intraocular Pressure
	SBP	Systolic Blood Pressure
	DBP	Diastolic Blood Pressure
	MAP	Mean Arterial Pressure
	HR	Heart Rate
Physiology-Enhanced Features	Q	Total retinal blood flow
	P_1	Average blood pressure in the central retinal artery
	P_2	Average blood pressure in retinal arterioles
	P_4	Average blood pressure in retinal venules
	P_5	Average blood pressure in the central retinal vein
	R_4	Average resistance in retinal venules
	R_5	Average resistance in the central retinal vein

FCM requires two parameters to be set *a priori*, namely the degree of fuzziness, m, and the number of clusters, C. In the absence of better knowledge, m is commonly set to 2 [61]; this is the value adopted in this study. The choice of C leads to the classical question of determining the optimal number of clusters that best complies with the structure of the clustered data. This problem is referred to as cluster validity and can be addressed using cluster validity indices (CVIs). A CVI is commonly defined as a function of intra-cluster cohesion (within-group scatter) and inter-cluster separation (between-group scatter) to estimate the quality of a clustering partition. The CVI usually reaches its maximum or minimum value when the "correct" number of well-separated clusters is found, meaning that the intra-cluster compactness is preserved while also increasing inter-cluster separability. A common method to get the optimal number of clusters C is as follows: (i) run the clustering algorithm on the given dataset multiple times with different values of C; (ii) calculate the CVI from the final partition produced by each run; (iii) take the value of C corresponding to the maximum (or minimum) value of the CVI as the optimal number of clusters. In this paper, we use two CVIs, namely the Xie-Beni index, defined as the quotient between the total mean squared error and the minimum separation (distance between prototypes) of the clusters [34], and the Davies-Bouldin index, defined as the quotient between the mean distance of data samples to their respective cluster prototype and the distance between cluster prototypes [35].

FCM also requires a random initialization, which may lead to different outcomes if the cluster structure within the dataset is not robust. Thus, in this study we test the cluster stability with respect to

the initialization in order to ensure that the clusters identified via FCM are actually capturing inherent structures of the dataset and not mere numerical artifacts.

2.4. Glaucoma progression markers

Due to its longitudinal design, the IGPS dataset offers a unique opportunity to investigate how belonging to a certain cluster at the baseline visit correlates with glaucoma progression. It is important to note that multiple definitions of glaucoma progression have been utilized in the clinical literature to capture changes in structure and visual function. The progression criteria utilized in this work are consistent with previous clinical studies analyzing the IGPS dataset [36].

Structural progression is defined as two consecutive visits with an average RNFL thickness decrease $\geq 8\%$, and/or horizontal or vertical C/D ratio increase by ≥ 0.2 from baseline [36]. Functional progression is defined as two consecutive visits with a decrease of 2 dB or more in visual field mean deviation (MD) compared to baseline [36]. The definitions of structural and functional progression given above require each eye to have at least two consecutive visits. Thus, eyes were discarded from the analysis if they did not meet this requirement. To mitigate the risks of false positives, the overall trend of these markers over time was considered. Specifically, for RNFL-based progression, confirmed progressors were those exhibiting a negative correlation (Spearman's rank correlation coefficient $r < -0.3$) between average RNFL and time. For C/D ratio-based progression, confirmed progressors were those exhibiting a positive correlation ($r > 0.3$) between C/D ratios and time. Confirmed progressors were those exhibiting a negative correlation ($r < -0.3$) between MD and time. Only correlations with p-values < 0.01 were considered statistically significant for changes in clinical markers over time.

Based on these definitions, among all eyes in the IGPS dataset, 10% progressed structurally, 22% progressed functionally, and 4% progressed both structurally and functionally.

3. Results

The DT-OH approach is applied to the IGPS dataset to identify IOP-MAP that could be more indicative of glaucoma progression. After enhancing the dataset with the physiology-based model outcomes (Section 3.1), the structure of the dataset and its cluster tendency are explored (Section 3.2). The relationship between cluster membership at baseline and structural and functional progression over four years is investigated (Section 3.3). Next, the clusters are analyzed with respect to their characteristic features, which enables physiology-based hemodynamic profiling based on specific IOP-MAP combinations (Section 3.4).

3.1. Physiology-based dataset enhancement

Figure 5(a) displays the values measured in each eye as a point in the two-dimensional (2-D) plane with IOP and MAP on the horizontal and vertical axes, respectively. The graph appears as a cloud of dispersed points, without obvious clusters. We further analyzed the distributions of MAP and IOP by visualizing the frequency histogram plots, see Figure 5(d) and Figure 5(e), and the normal probability plots, see Figure 5(b) and Figure 5(c). These results suggest that, when considered independently, the values of MAP and IOP appear reasonably normally distributed.

The 3-D visualization of the distribution of the physiology-enhanced variables obtained with the mathematical model based on individualized inputs of SBP, DBP, HR, and IOP shows interesting re-

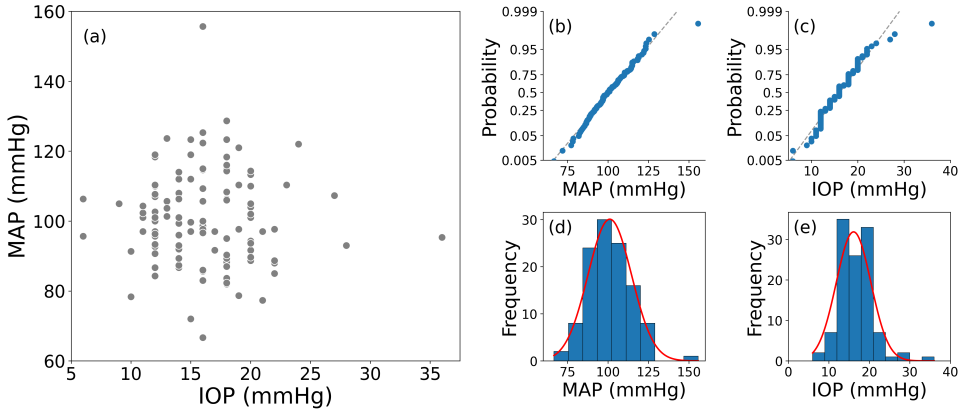

Figure 5. (a) Two-dimensional plot of the values of mean arterial pressure (MAP) and intraocular pressure (IOP) for all eyes at their baseline visit of the Indianapolis Glaucoma Progression Study (IGPS); (b,c) normal probability plots for MAP and IOP for all eyes at their baseline IGPS visit; (d,e) frequency histogram plots for MAP and IOP for all eyes at their baseline IGPS visit.

sults, see Figure 6. Frequency histogram plots are portrayed for the distributions of MAP and IOP, see Figure 6(a), vascular resistance in the venules (R_4) and IOP, see Figure 6(b), and vascular resistance in the CRV (R_5) and IOP, see Figure 6(c). The highly nonlinear relationship between MAP, IOP, and the model-estimated variables results in a non-uniform "shift" of the histogram plots relative to the IOP-MAP histograms in Figure 6(a). That is, while Figure 6(a) shows a centered bell shape for the IOP-MAP frequency bars, the plots for the R_4-IOP and R_5-IOP plots appear to be shifted along a line, see Figure 6(b), or toward the left, see Figure 6(c). These shifts indicate that the mathematical model has performed a nonlinear transformation of the clinical input variables and suggests that eyes that are relatively "close" in terms of their MAP and IOP values can actually experience very different hemodynamic conditions due to the highly nonlinear effects that specific IOP-MAP combinations have on the blood circulation. This provides motivation for considering the clustering of eyes with the physiology-enhanced features.

3.2. Exploration of cluster tendency

Figure 7 displays the results obtained by running the FCM algorithm with $C = 3$ and $m = 2$ in the 12-D physiology-enhanced baseline dataset within IGPS and carrying the hardened cluster labels into the projection space. Figure 7(a) reports a popular cluster visualization based on a non-linear 3-D projection of the 12-D enhanced feature vectors, known as t-distributed stochastic neighbor embedding (t-SNE), which projects the data points from the original 12-D space onto a 3-D space. While the axes are unit-less and do not carry any clinical meaning, they help us visualize the separable structures that may exist in the 12-D feature space in 3-D, marked by the three distinct colors in Figure 7(a). The figure suggests that when MAP and IOP are considered along with the impact that they have on ocular circulation, as quantified via the features from the mathematical model, a cluster structure is unveiled and it is separable in the 12-D feature space. Figure 7(b) shows the same 3 clusters projected on the IOP-MAP plane for clinical interpretation and relevance.

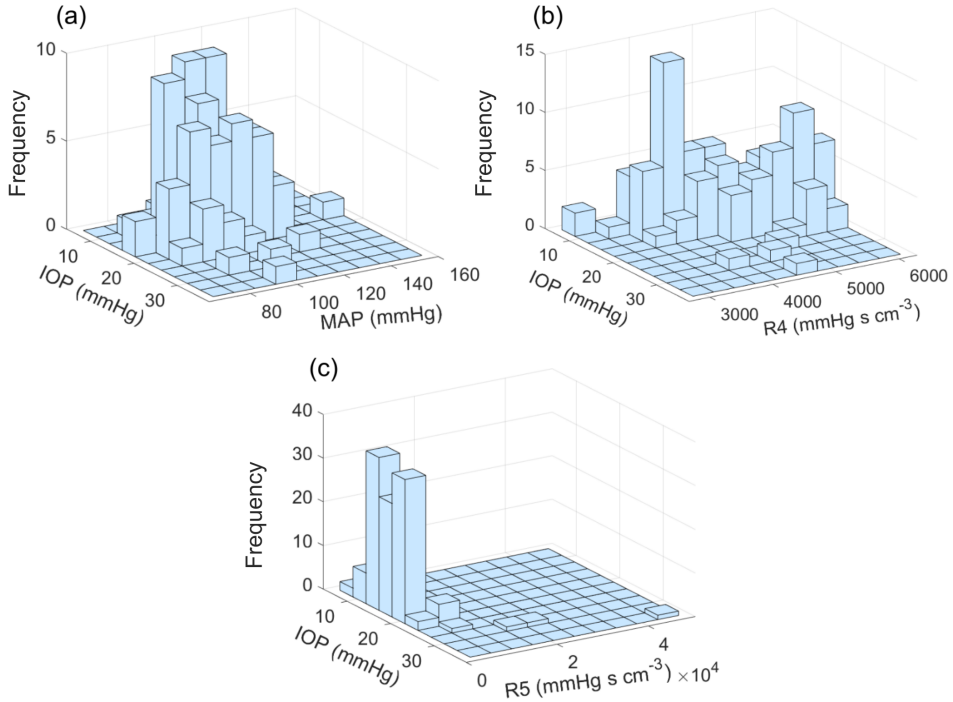

Figure 6. Three-dimensional visualization of the distribution of mean arterial pressure (MAP) and two physiology-enhanced variables (vascular resistance in the venules (R_4) and in the CRV (R_5)) with respect to intraocular pressure (IOP).

After performing 10 FCM runs with randomly initialized cluster centers and iteratively updating the centers and membership degrees until convergence, the resulting cluster centers derived from the 12-D feature set exhibited minimal variation. Figure 8(a) shows cluster centers in the IOP-MAP plane,

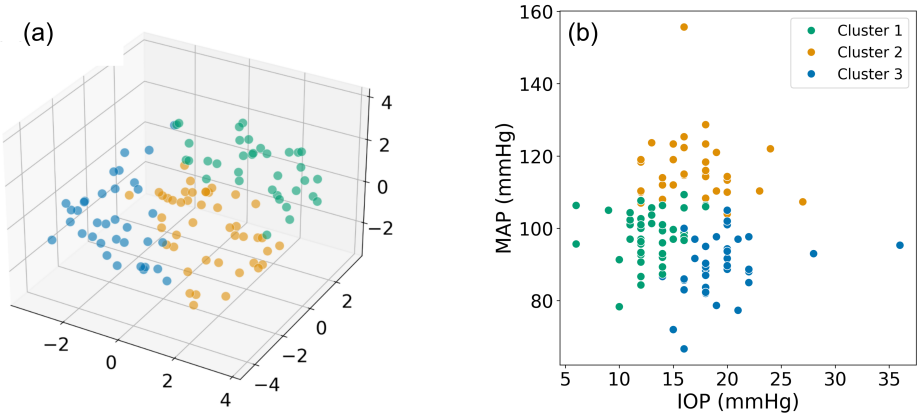

Figure 7. Clustering results obtained by applying FCM with $C = 3$ and $m = 2$ to the 12-D physiology-enhanced baseline dataset within IGPS. Results are displayed via t-distributed stochastic neighbor embedding (t-SNE) visualization (a) and via a projection on the IOP-MAP plane (b) for clinical interpretation, carrying the hardened cluster labels into the projection space.

highlighting the stability of cluster centers across the different runs when the full 12-D feature set was used. In stark contrast, when clustering was performed using only IOP and MAP values, see Figure 8(b), the cluster centers varied significantly and lacked a clear separation.

These results provide confidence in the stability of the FCM clusters obtained for the 12-D physiology-enhanced dataset, but not for the case in which IOP and MAP are considered as stand-alone values without physiology-based model enhancement.

Figure 9 shows the hardened and soft memberships for all eyes in each cluster. We recall that the clustering occurs in the 12-D space and then the results are projected into the 2-D IOP-MAP plane; this explains why the membership distributions appear more complex than a simple spatial gradient.

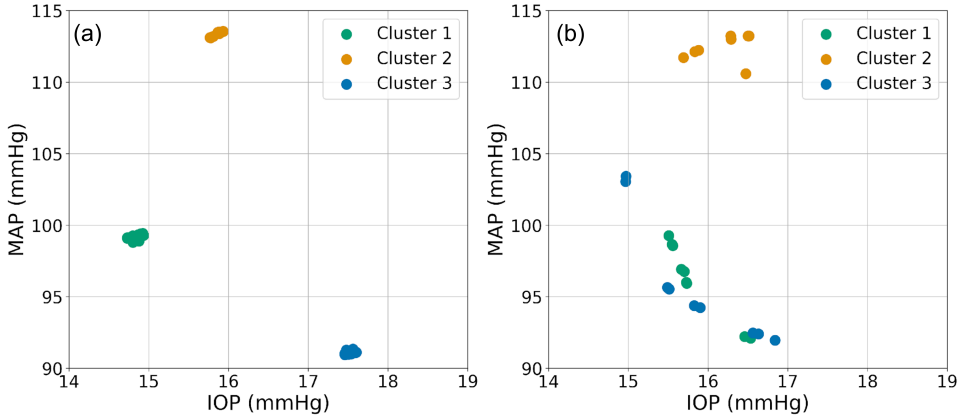

Figure 8. Cluster stability analysis with respect to FCM initialization was performed on the baseline dataset in two cases: (a) all 12-D features were considered, including the physiology-enhanced variables; (b) only IOP and MAP were considered, without the physiology-enhanced variables.

Figure 10 shows the Xie-Beni and Davies-Bouldin indices, as the number of clusters, C, is varied between 2 and 9. For each value of C, FCM was run 100 times on the 12-D enhanced dataset of the 114 eyes in the IGPS study. For each run, the initialization of the first cluster centers was done randomly from the data. The Xie-Beni and Davies-Bouldin indices were calculated from the final partition from each run. The validity indices for each C represent the average of all 100 runs, and the vertical bar represents the standard deviation. Validity measures, while very useful guidelines, are not absolute rules; they have their own assumptions and parameters. Both indices show $C = 2$ is favored. However, from a practical standpoint, $C = 2$ for the IGPS data, when projected back onto the IOP-MAP plane splits the eyes into low BP vs. high BP, with no influence of IOP. Considering that elevated IOP is the only treatable risk factor for glaucoma, this option limits the underlying potential for studying glaucoma progression. While the validity measures of $C = 3$ and $C = 4$ are close, $C = 4$ could lead to very small partitions in a dataset of only 114 data points, thereby reducing the power of subsequent statistical analyses. Hence, in this study, we have analyzed the cluster structure found with $C = 3$.

3.3. Clustering and glaucoma progression

The main question addressed in this section is whether the clusters are indicative of glaucoma risk. To this end, we consider the definitions of structural and functional progression given in Section 2.4 and we apply them to the eyes in each cluster. Figure 11 reports the percentage of eyes that progressed

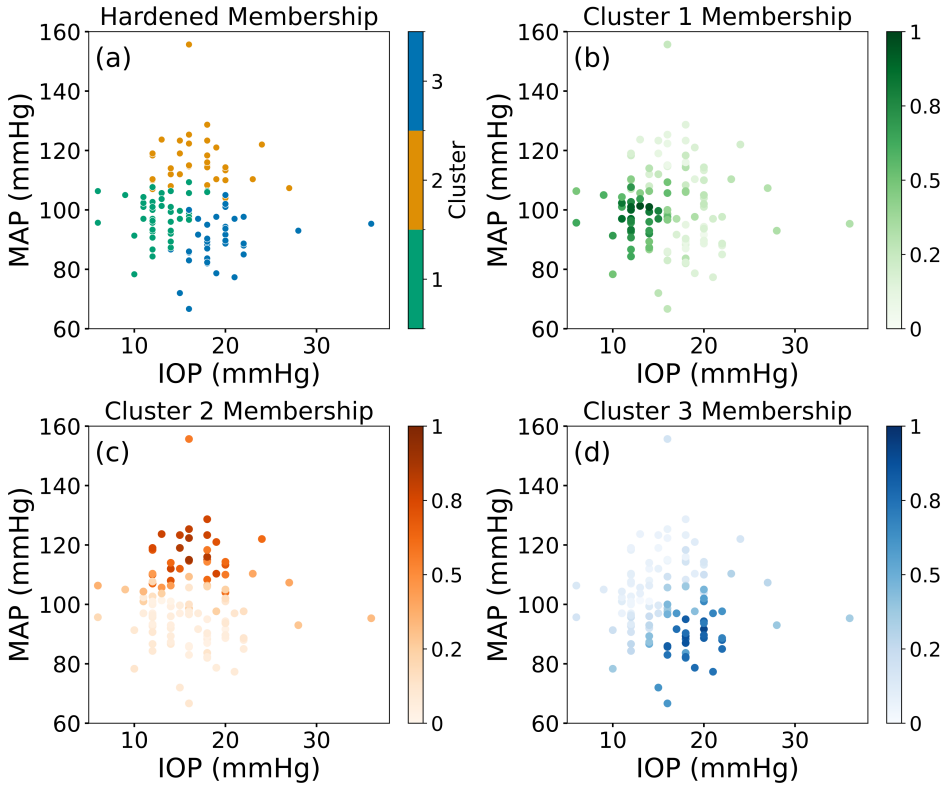

Figure 9. Hardened memberships (a) and soft memberships (b,c,d) for all eyes in each cluster projected onto the IOP-MAP plane.

structurally (a), functionally (b), or both (c), when all IGPS eyes are considered as a single group (red dashed lines) or by cluster (color bars). Height and whiskers of the color bars represent median and 25/75 percentiles over 100 FCM runs, respectively. The analysis is performed over multiple runs to ensure the robustness of the results with respect to the random FCM initialization. Overall, results in Figure 11 suggest that:

- *Cluster 1 may be a relatively "safer zone" with respect to structural and functional progression*

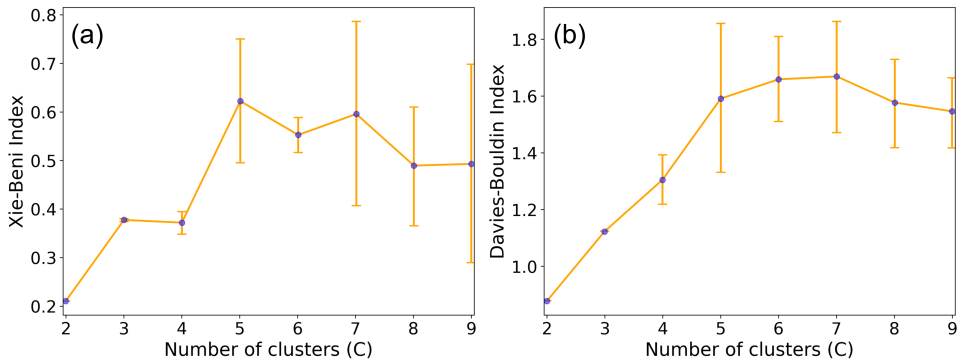

Figure 10. Xie-Beni (a) and Davies-Bouldin (b) cluster validity measures for 100 runs of FCM on the IGPS data for $C = 2$ to $C = 9$, with $m = 2$.

when considered separately Figure 11(a,b) or in combination Figure 11(c). The median values of structural, functional, and combined progressors in Cluster 1 are 8.8%, 16.5%, and 2.9%, respectively, which are lower than those obtained when all eyes are considered together.

- *Cluster 2 may be a relatively "riskier zone" with respect to structural and functional progression when considered separately Figure 11(a,b) or in combination Figure 11(c).* The median values of structural, functional, and combined progressors in Cluster 2 are 16.2%, 31.9%, and 6.1%, respectively, which are higher than those obtained when all eyes are considered together.
- *Cluster 3 may be a relatively "riskier zone" with respect to functional progression Figure 11(b).* The median value of functional progressors in Cluster 3 is 23.8%, which is higher than that obtained when all eyes are considered together.

3.4. Physiology-based hemodynamic profiling

The results of Section 3.3 suggest that eyes in Cluster 1 may be at lower risk for glaucoma progression than those in Clusters 2 and 3. Here, we analyze the clusters with respect to their characteristic features. This important aspect of the DT-OH approach enables physiology-based hemodynamic profiling of eyes based on their specific IOP-MAP combinations.

Figure 12 summarizes the median values of the 12 features in the physiology-enhanced dataset used for clustering, see Table 2, using a heatmap visualization. Each cell corresponds to the median value of a specific feature (row) in one of the three clusters (column), and the intensity of the color visualizes the feature magnitude as specified by the colorbars. It is interesting to notice that Cluster 3 is characterized by high IOP and low MAP, resulting in higher values of the venous resistances R_4 and R_5 and lower values of blood flow Q. Thus, the eyes in Cluster 3 may be in a condition of low flow and high resistance, which might make them more vulnerable to ischemia. In contrast, Cluster 2 is characterized

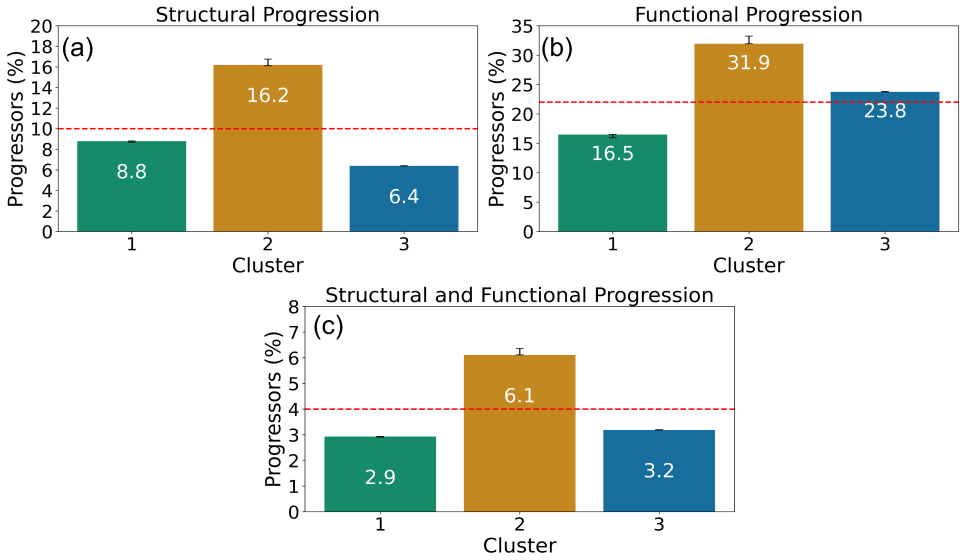

Figure 11. Bar graphs showing results for (a) structural, (b) functional, and (c) structural and functional progression across 100 FCM runs. Bar height represents the median, and the whiskers represent the 25/75 quartiles across runs for each cluster. The results obtained when all IGPS eyes are considered as a single group are also reported (red dashed lines).

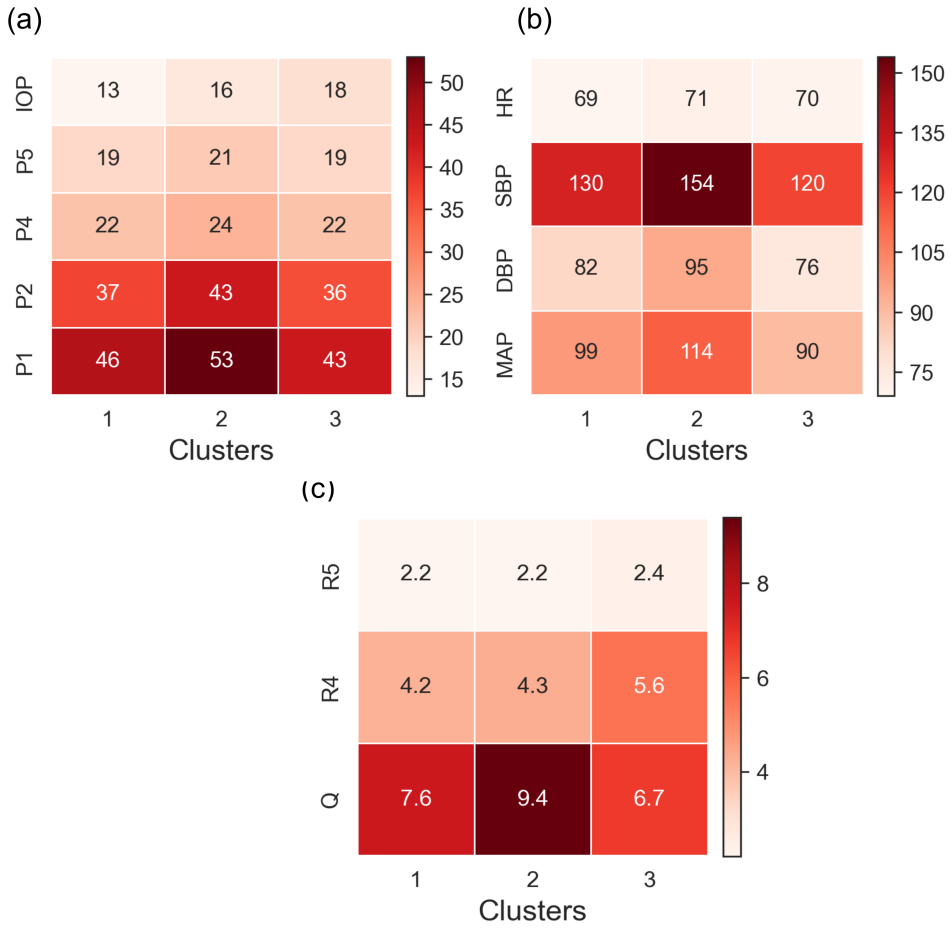

Figure 12. Heatmaps showing the medians of the features in the physiology-enhanced dataset for each cluster. Specifically, the figure shows the median values of IOP and the pressures throughout the retinal vasculature (P_1, P_2, P_4, P_5) [mmHg] (a); systolic, diastolic, and mean arterial pressures (SBP, DBP, MAP) [mmHg], and heart rate (HR) [bpm] (b); vascular resistances (R_4, R_5) [10^3 mmHg s ml^{-1}] and total retinal blood flow (Q) [10^{-4} ml s^{-1}].

by high MAP, which results in higher values for the total retinal blood flow Q since autoregulatory effects are switched off in the model. We recall that this has been an intentional choice, meaning that the physiology-based mathematical model is purposely run without accounting for autoregulation so that pressure-driven blood flow changes are unmasked. In other words, the higher Q values estimated by the model are unmasking the extent by which vascular regulation may be engaged to compensate the higher MAP values characterizing the eyes in Cluster 2. As a result of this underlying regulatory engagement, the capability of the vasculature to adjust for physiological variations in BP and IOP may be reduced. These findings support the formulation of the following hypotheses:

- When MAP is high, regardless of IOP, the arterial side of the circulation may be heavily recruited in blood flow regulation, thereby limiting its capacity to compensate for inevitable variations in BP and IOP due to, for example, the circadian rhythm or activity levels. Thus, *we hypothesize that the compromised capacity of arterial regulation may be driving glaucoma progression in eyes*

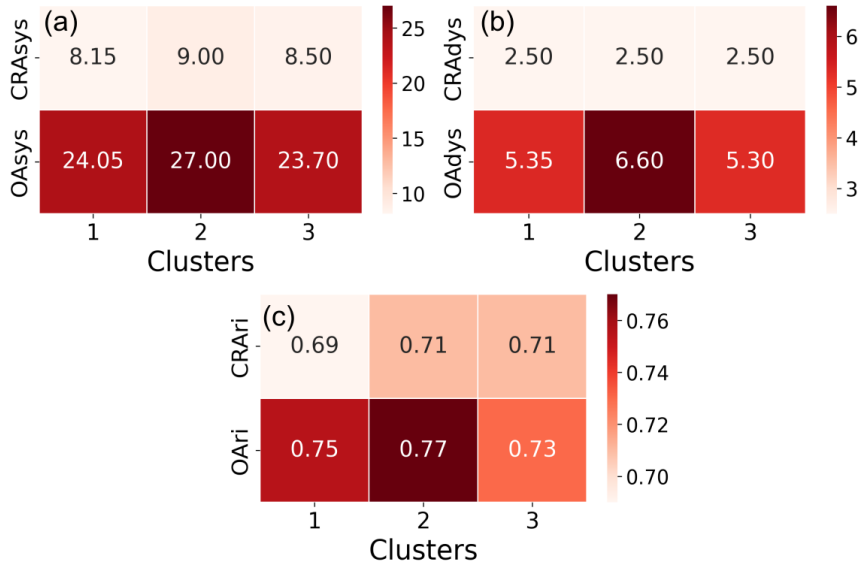

Figure 13. Heatmaps (a), (b), and (c) show the median peak systolic velocity [$cm\ s^{-1}$], peak diastolic velocity [$cm\ s^{-1}$], and the resistivity index [−] in the CRA and OA for each cluster.

that at baseline belong to Cluster 2.

- When MAP is low and IOP is high, as it happens in Cluster 3, the venous side of the circulation may be experiencing a higher degree of external compression, thereby increasing venous resistance and the venous susceptibility to collapse. Thus, *we hypothesize that the venous compression vulnerability may be driving glaucoma progression in eyes that at baseline belong to Cluster 3.*

The plausibility of the aforementioned hypotheses is explored by comparing the cluster characteristic values of OAsys, OAdys, OAri and CRAsys, CRAdys, CRAri. The results are reported in the heatmaps in Figure 13. The values of OAsys and OAdys are notably higher for eyes in Cluster 2 when compared to those in Clusters 1 and 3 (Figure 13(a,b)). However, in the CRA, CRAdys of eyes in Cluster 2 are comparable to those in Clusters 1 and 3 (Figure 13(b)). The similarity in CRA velocities despite higher OA velocities could be reflecting a more prominent engagement of vascular regulation in the retinal circulation for the eyes in Cluster 2. This could, in turn, limit their capacity to compensate for physiological pressure fluctuations, thereby leaving them more vulnerable to damage. Interestingly, the CRAri and OAri in both Clusters 2 and 3 are higher than in Cluster 1 (Figure 13(c)). This difference points to a higher resistance to blood flow in both Clusters 2 and 3. However, CRAsys and both OAsys and OAdys differ more between Clusters 1 and 2, than Clusters 1 and 3, thereby suggesting that a different factor may be causing the increased resistance. Our DT-OH approach indicates that such a mechanism may be related to an increased venous compression, but direct clinical data on venous hemodynamic imaging in the eye are not fully developed yet.

4. Discussions

The proposed DT-OH approach is highly novel as it combines different modeling approaches (physiology-based mathematical modeling and machine learning methods), each being used in a different and complementary way. In this approach, the digital twin of an eye consists of: *i)* the individual

specific values of IOP, BP, and HR, and the associated physiology-based model estimates of vascular pressures, resistances, and flow rates; and *ii)* the cluster label for hemodynamic status and glaucoma risk profiling. The method builds on the foundation of computational modeling and digital-twin paradigms described in [23], which advocate for combining biophysical and data-driven methods in healthcare. Previous approaches to understand hemodynamic responses in different parts of the body include animal models [58], and bias-prone imaging techniques [59]. Previous applications of machine learning and AI in glaucoma research have predominantly focused on neural network performance, often with limited emphasis on physiological interpretability [60]. Our approach leverages a fully in silico digital twin, enabling noninvasive and objective analysis of hemodynamic status and personalized glaucoma risk profiling, while additionally providing physiologically grounded explanations for the outcomes. Physiology-based mathematical modeling is used to quantify the hemodynamic status associated with specific combinations of IOP, BP, and HR. Given that measurements of IOP, BP, and HR are available to virtually any clinic, the outcomes of our analyses have immediate clinical relevance and could be implemented even in clinics that do not have access to advanced imaging techniques. Machine learning methods are used to identify eyes for which specific combinations of IOP, BP, and HR yield a similar hemodynamic status in the retina. The application of machine learning techniques in ophthalmology has gained significant traction in recent years, with applications focusing mostly on glaucoma diagnosis and prediction of progression based on imaging data [37–41]. The richness of the approach presented in this study lies in the enhancement of the standard clinical measurements with hemodynamic variables generated by a validated physiology-based mathematical model of blood flow in the eye [26]. The stability analysis with respect to FCM initialization has revealed that this enhancement is crucial to achieve stable clustering.

The proposed DT-OH approach applied to IGPS proved capable of identifying specific eye profiles that are indicative of different degrees of glaucoma progression, based on their IOP and BP values at baseline.

Interestingly, two profiles are found to be at higher risk for progression, namely those corresponding to Cluster 2 and Cluster 3, but for different reasons. Eyes in Cluster 3 may be characterized by higher venous resistances, whereas eyes in Cluster 2 may be experiencing limited regulation capacity. These findings are consistent with those of Pappelis et al. [42], who used a similar rationale to model the BP and IOP limits outside which autoregulation fails and the retina could undergo hypoperfusion. In a subsequent publication [43], the authors used these predictions and showed that BP status, especially intensively treated hypertensives, and autoregulation limits were indeed correlated with ganglion cell thickness. Carichino et al. analyzed velocity waveforms obtained with color doppler imaging and found that glaucoma patients with higher BP have a higher peak systolic velocity in the ophthalmic artery (OAsys) [57]. Additionally, a higher resistivity index in the ophthalmic artery (OAri) measured via color doppler imaging has previously been linked to a higher likelihood of visual field deterioration, as shown by Galassi et al. in [56], where the odds of deterioration for patients with OAri ≥ 0.78 were found to be six times higher than those with lower OAri.

The discovery of clinically meaningful subgroups of patients in a dataset is essential for developing precision in therapy. Statistical analysis based on cohorts, groups, or classes is often performed to investigate whether relationships between clinical markers are more pronounced in certain groups than in others. Unsupervised cluster analysis has been an important data-based approach to find such retrospective or post-hoc subgroups in observational studies, see, e.g., Alashwal et al. [44] and the

references therein. The novelty of our work lies in the choice of variables used in the cluster analysis, which include a subset of the clinical data (BP, IOP, HR) augmented by hemodynamic features (vascular pressure, flow, vascular resistance) that are estimated using a validated mathematical model based on physiology [20]. The rationale for our approach is twofold: (i) it is based on simple measurements available virtually anywhere (IOP and BP), and (ii) it uses the imaging data only for a-posteriori assessment of progression and not for cluster building. In so doing, the outcomes of our approach are broadly accessible for clinics that may not have access to the new cutting-edge imaging technologies.

This work focuses on the IGPS study, which provides valuable multimodal longitudinal clinical data for glaucoma patients evaluated at the same clinic by the same operators. However, only 114 eyes are included in IGPS. Although this is a relatively small sample size it is fairly typical of studies on conditions with low incidence, such as glaucoma. Indeed, even large population-based studies with patients numbering in the thousands have comparable sample sizes to the ones used here. For example, Singapore Epidemiology of Eye Diseases (SEED) included a total of 19,587 eyes, among which only 293 had glaucoma [28, 29]. The Thessaloniki Eye Study included 2261 subjects and only 135 had glaucoma [45].

Testing the findings of this study on larger datasets that include multiple longitudinal assessments of glaucoma progression would be the next step.

In the present analysis, baseline values refer to those measured during the first visit at which a patient entered the IGPS. While the IGPS was designed to ensure homogeneity in terms of disease stage, this might not be the case in the population. Hence, examining the temporal trajectories of each eye's physiology-enhanced features and potential transitions between clusters could reveal whether dynamic changes in ocular hemodynamics are predictive of structural or functional progression. Incorporating such temporal analyses represents an important next step toward extending the DT-OH framework from static risk profiling to dynamic modeling of glaucoma evolution.

Beyond its value for disease stratification, the clustering framework developed here has potential applications in personalized medicine in a clinical setting. Once a patient's IOP, BP, and HR are measured, they can be used to assign the patient to one of the identified clusters in the IOP-MAP plane. This classification may help tailor management strategies for said patient based on their hemodynamic profile. In a preliminary external evaluation of the findings using the SEED cohort, the clusters derived from IGPS were transferred using feature-alignment techniques. Eyes corresponding to Cluster 2 in SEED exhibited the greatest decline in VF (measured using MD) over time, despite concomitant lowering of both IOP and BP. In contrast, eyes in Cluster 3, whose management emphasized IOP reduction, showed no significant decline in VF. Lastly, eyes in Cluster 1, which did not receive aggressive therapeutic interventions, also remained stable [62]. These findings suggest that distinct hemodynamic profiles may respond differently to therapy, underscoring the potential of DT-OH-based stratification to guide personalized treatment decisions.

Currently, the only approved modifiable risk factor for glaucoma is IOP, which can be reduced pharmaceutically or surgically. Thus, if the results on IOP-BP profiling enabled by DT-OH is confirmed in multi-center, large-scale, longitudinal progression studies, these findings would provide a practical way to guide individualized approaches for glaucoma care accounting for both IOP and BP.

5. Conclusions

The enigma preventing translation of BP outcomes for enhancing glaucoma care has a significant impact due to the high prevalence of hypertension and hypertensive treatments in the US and worldwide populations [46–49]. It is important to note that BP-related disease impact involves significant disparities based on sex, age, race, and reported ethnicities [47–55]. Clustering analysis is highly useful in such situations to help identify those groups of patients with shared variables and elevated risk of disease onset and progression. Clusters are especially meaningful when data-driven analysis from targeted clinical studies with comprehensive assessments may be applied to larger population-based studies that lack specific imagery or diagnostic capabilities.

Finally, we acknowledge that, despite its usefulness, the mathematical model utilized in this study has several limitations, including the fact that it does not account for the circulation within the optic nerve head or include oxygen transport across the vessels and tissues. The overall multistep approach, though, is modular and it lends itself to swap the mechanistic module with more advanced physiology-based models as they become available.

Use of AI tools declaration

The authors declare they have not used Artificial Intelligence (AI) tools in the creation of this article.

Acknowledgments

This work has been partially supported by NIH R01EY030851, NIH R01EY034718, NSF-DMS 2108711/2327640, NYEE Foundation grants, The Glaucoma Foundation, the Barry Family Center for Ophthalmic Artificial Intelligence & Human Health at Mount Sinai Hospital, and in part by a Departmental Challenge Grant award from Research to Prevent Blindness, NY. We are grateful to Ms. Jill Gregory for the graphic illustrations.

Conflict of interest

Professor Alon Harris would like to disclose that he received remuneration from AdOM, Qlaris, and Cipla for serving as a consultant, and he serves on the board of AdOM, Qlaris and SlitLed. Professor Alon Harris holds an ownership interest in AdOM, Oxymap, Qlaris, SlitLed, and AEYE Health. If you have questions regarding paid relationships that your physician/researcher may have with industry, you are encouraged to talk with your physician/researcher, or check for industry relationships posted on individual faculty pages on our website at `http://icahn.mssm.edu/`.

References

1. A. Heijl, M. C. Leske, B. Bengtsson, L. Hyman, B. Bengtsson, M. Hussein, et al., Reduction of intraocular pressure and glaucoma progression: Results from the Early Manifest Glaucoma Trial, *Arch. Ophthalmol.*, **120** (2002), 1268–1279. https://doi.org/10.1001/archopht.120.10.1268

2. A. Harris, G. Guidoboni, B. Siesky, S. Mathew, A. C. Verticchio Vercellin, L. Rowe, et al., Ocular blood flow as a clinical observation: Value, limitations and data analysis, *Prog. Retin. Eye Res.*, **78** (2020), 100841. https://doi.org/10.1016/j.preteyeres.2020.100841

3. R. N. Weinreb, A. Harris, *Ocular blood flow in glaucoma: The 6th consensus report of the world glaucoma association*, Kugler Publications, Amsterdam, **6** (2009). Available from: https://wga.one/consensus/consensus-6

4. M.C. Leske, A. Heijl, M. Hussein, B. Bengtsson, L. Hyman, E. Komaroff, et al., Factors for glaucoma progression and the effect of treatment: The Early Manifest Glaucoma Trial, *Arch. Ophthalmol.*, **121** (2003), 48–56. https://doi.org/10.1001/archopht.121.1.48

5. R. N. Weinreb, C. K. Leung, J. G. Crowston, F. A. Medeiros, D. S. Friedman, J. L. Wiggs, et al., Primary open-angle glaucoma, *Nat. Rev. Dis. Primers*, **2** (2016), 1–19. https://doi.org/10.1038/nrdp.2016.67

6. R. N. Weinreb, T. Aung, F. A. Medeiros, The pathophysiology and treatment of glaucoma: A review, *JAMA*, **311** (2014), 1901–1911. https://doi.org/10.1001/jama.2014.3192

7. Y. J. Lim, J. W. Bang, R. N. Weinreb, L. M. Zangwill, M. H. Suh, Temporal optic disc microvasculature dropout in glaucoma, *Invest. Ophthalmol. Vis. Sci.*, **64** (2023), 6. https://doi.org/10.1167/iovs.64.11.6

8. V. P. Costa, J. Jimenez-Roman, F. G. Carrasco, A. Lupinacci, A. Harris, Twenty-four hour ocular perfusion pressure in primary open-angle glaucoma, *Br. J. Ophthalmol.*, **94** (2010), 1291–1294. https://doi.org/10.1136/bjo.2009.167569

9. H. J. Kaiser, J. Flammer, T. Graf, D. Stümpfig, Systemic blood pressure in glaucoma patients, *Graefe's Arch. Clin. Exp. Ophthalmol.*, **231** (1993), 677–680. https://doi.org/10.1007/bf00919280

10. B. Krasinska, M. Karolczak-Kulesza, Z. Krasinski, K. Pawlaczyk-Gabriel, A. Niklas, J. Głuszek, et al., A marked fall in nocturnal blood pressure is associated with the stage of primary open-angle glaucoma in patients with arterial hypertension, *Blood Pres.*, **20** (2011), 171–181. https://doi.org/10.3109/08037051.2010.538964

11. P. Mitchell, W. Smith, K. Attebo, P. R. Healey, Prevalence of open-angle glaucoma in Australia: The Blue Mountains Eye Study, *Ophthalmology*, **103** (1996), 1661–1669. https://doi.org/10.1016/S0161-6420(96)30449-1

12. I. Dielemans, J. R. Vingerling, D. Algra, A. Hofman, D. E. Grobbee, P. T. V. M. de Jong, Primary open-angle glaucoma, intraocular pressure, and systemic blood pressure in the general elderly population: The Rotterdam Study, *Ophthalmology*, **102** (1995), 54–60. https://doi.org/10.1016/s0161-6420(95)31054-8

13. P. J. Foster, D. Machin, T. Y. Wong, T. P. Ng, J. F. Kirwan, G. J. Johnson, et al., Determinants of intraocular pressure and its association with glaucomatous optic neuropathy in Chinese Singaporeans: The Tanjong Pagar Study, *Invest. Ophthalmol. Vis. Sci.*, **44** (2003), 3885–3891. https://doi.org/10.1167/iovs.03-0012

14. J. Y. Lee, J. A. Choi, Risk factors for disease progression in glaucoma patients with disk hemorrhage, *J. Glaucoma*, **33** (2024), 828–834. https://doi.org/10.1097/ijg.0000000000002460

15. V. Q. Pham, T. Nishida, S. Moghimi, C. A. Girkin, M. A. Fazio, J. M. Liebmann, et al., Long-term blood pressure variability and visual field progression in glaucoma, *JAMA Ophthalmol.*, **143** (2024), 25–32. https://doi.org/10.1001/jamaophthalmol.2024.4868

16. S. Y. Lee, J. S. Lee, J. Y. Kim, H. Tchah, H. Lee, Visit-to-visit variability in blood pressure and the risk of open-angle glaucoma in individuals without systemic hypertension: A nationwide population-based cohort study, *Front. Med.*, **10** (2024), 1300778. https://doi.org/10.3389/fmed.2023.1300778

17. J. D. Melgarejo, J. Van Eijgen, D. Wei, G. E. Maestre, L. A. Al-Aswad, C. T. Liao, et al., Effect of 24-h blood pressure dysregulations and reduced ocular perfusion pressure in open-angle glaucoma progression, *J. Hypertens.*, **41** (2023), 1785–1792. https://doi.org/10.1097/hjh.0000000000003772

18. J. Caprioli, A. L. Coleman, Blood pressure, perfusion pressure, and glaucoma, *Am. J. Ophthalmol.*, **149** (2010), 704–712. https://doi.org/10.1001/archopht.126.5.741-a

19. M. Fahim, V. Sharma, T. V. Cao, B. Canberk, T. Q. Duong, Machine learning-based digital twin for predictive modeling in wind turbines, *IEEE Access*, **10** (2022), 14184–14194. https://doi.org/10.1109/access.2022.3147602

20. A. Lal, G. Li, E. Cubro, S. Chalmers, H. Li, V. Herasevich, et al., Development and verification of a digital twin patient model to predict specific treatment response during the first 24 hours of sepsis, *Crit. Care Explor.*, **2** (2020), e0249. https://doi.org/10.1097/cce.0000000000000249

21. Q. Qiao, J. Wang, L. Ye, R. X. Gao, Digital twin for machining tool condition prediction. *Procedia CIRP*, **81** (2019), 1388–1393. https://doi.org/10.1016/j.procir.2019.04.049

22. R. Laubenbacher, B. Mehrad, I. Shmulevich, N. Trayanova, Digital twins in medicine, *Nat. Comput. Sci.*, **4** (2024), 184–191. https://doi.org/10.1038/s43588-024-00607-6

23. M. Laviola, Introduction to the special section on computational modeling and digital twin technology in biomedical engineering, *IEEE Open J. Eng. Med. Biol.*, **5** (2024), 607–610. https://doi.org/10.1109/ojemb.2024.3428898

24. G. A. Alsalloum, N. M. Al Sawaftah, K. M. Percival, G. A. Husseini, Digital twins of biological systems: A narrative review, *IEEE Open J. Eng. Med. Biol.*, (2024), 670–677. https://doi.org/10.1109/ojemb.2024.3426916

25. M. E. Iliuţă, M. A. Moisescu, S. I. Caramihai, A. Cernian, E. Pop, D. I. Chiş, et al., Digital twin models for personalised and predictive medicine in ophthalmology, *Technologies*, **12** (2024), 55–55. https://doi.org/10.3390/technologies12040055

26. G. Guidoboni, A. Harris, S. Cassani, J. Arciero, B. Siesky, A. Amireskandari, et al., Intraocular pressure, blood pressure, and retinal blood flow autoregulation: A mathematical model to clarify their relationship and clinical relevance, *Invest. Ophthalmol. Vis. Sci.*, **55** (2014), 4105–4118. https://doi.org/10.1167/iovs.13-13611

27. N. A. Moore, A. Harris, S. Wentz, A. C. V. Vercellin, P. Parekh, J. Gross, et al., Baseline retrobulbar blood flow is associated with both functional and structural glaucomatous progression after 4 years, *Br. J. Ophthalmol.*, **101** (2017), 305–308. https://doi.org/10.1136/bjophthalmol-2016-308460

28. Y. C. Tham, S. H. Lim, P. Gupta, T. Aung, T. Y. Wong, C. Y. Cheng, Inter-relationship between ocular perfusion pressure, blood pressure, intraocular pressure profiles and primary open-angle glaucoma: The Singapore Epidemiology of Eye Diseases study, *Br. J. Ophthalmol.*, **102** (2018), 1402–1406. https://doi.org/10.1136/bjophthalmol-2017-311359

29. S. Majithia, Y. C. Tham, M. L. Chee, S. Nusinovici, C. L. Teo, M. L. Chee, et al., Cohort profile: The Singapore Epidemiology of Eye Diseases study, *Int. J. Epidemiol.*, **50** (2021), 41–52. https://doi.org/10.1093/ije/dyaa238

30. G. Guidoboni, A. Harris, R. Sacco, *Ocular fluid dynamics*, Springer, New York, (2019). https://doi.org/10.1007/978-3-030-25886-3

31. R. Rai, G. Guidoboni, C. K. Wikle, F. Topouzis, B. Siesky, A. Verticchio Vercellin, et al., Retinal venous vulnerability in primary open angle glaucoma: The combined effects of intraocular pressure and blood pressure with application to the Thessaloniki Eye Study, *La Matematica*, **4** (2024), 66–83. https://doi.org/10.1007/s44007-024-00144-8

32. J. Keller, M. Gray, J. Givens, A fuzzy K-nearest neighbor algorithm, *IEEE Trans. Syst. Man. Cybern.*, **15** (1985), 580–585. https://doi.org/10.1109/tsmc.1985.6313426

33. N. R. Pal, K. Pal, J. M. Keller, J. C. Bezdek, A possibilistic fuzzy c-means clustering algorithm, *IEEE Trans. Fuzz. Syst.*, **13** (2005), 517–530. https://doi.org/10.1109/tfuzz.2004.840099

34. X. L. Xie, G. Beni, A validity measure for fuzzy clustering, *IEEE Trans. Pattern Anal. Mach. Intell.*, **13** (2002), 841–847. https://doi.org/10.1109/34.85677

35. D. L. Davies, D. W. Bouldin, A cluster separation measure, *IEEE Trans. Pattern Anal. Mach. Intell.*, **2** (2009), 224–227. https://doi.org/10.1109/TPAMI.1979.4766909

36. A. C. Vercellin, A. Harris, F. Oddone, B. Siesky, G. Eckert, A. Belamkar, et al., Ocular blood flow biomarkers may predict long-term glaucoma progression, *Br. J. Ophthalmol.*, **108** (2024), 946–950. https://doi.org/10.1136/bjo-2022-322644

37. P. Murtagh, G. Greene, C. O'Brien, Current applications of machine learning in the screening and diagnosis of glaucoma: A systematic review and meta-analysis, *Int. J. Ophthalmol.*, **13** (2020), 149–162. https://doi.org/10.18240/ijo.2020.01.22

38. M. H. Goldbaum, P. A. Sample, K. Chan, J. Willians, T. Lee, E. Blumenthal, et al., Comparing machine learning classifiers for diagnosing glaucoma from standard automated perimetry, *Invest. Ophthalmol.Vis. Sci.*, **43** (2002), 162–169. Available from: https://pubmed.ncbi.nlm.nih.gov/11773027

39. R. Nunez, A. Harris, O. Ibrahim, J. Keller, C. K. Wikle, E. Robinson, et al., Artificial intelligence to aid glaucoma diagnosis and monitoring: State of the art and new directions, *Photonics*, **9** (2022), 810. https://doi.org/10.3390/photonics9110810

40. N. Riina, A. Harris, B. A. Siesky, L. Ritzer, L. R. Pasquale, J. C. Tsai, et al., Using multi-layer perceptron driven diagnosis to compare biomarkers for primary open angle glaucoma, *Invest. Ophthalmol. Vis. Sci.*, **65** (2024), 16. https://doi.org/10.1167/iovs.65.11.16

41. M. Aloudat, M. Faezipour, A. El-Sayed, Automated vision-based high intraocular pressure detection using frontal eye images, *IEEE J. Transl. Eng. Health Med.*, **7** (2019), 1–13. https://doi.org/10.1109/jtehm.2019.2915534

42. K. Pappelis, L. Choritz, N. M. Jansonius, Microcirculatory model predicts blood flow and autoregulation range in the human retina: In vivo investigation with laser speckle flowgraphy, *Am. J. Physiol. Heart Circ. Physiol.*, **319** (2020), H1253–H1273. https://doi.org/10.1152/ajpheart.00404.2020

43. K. Pappelis, N. M. Jansonius, U-shaped effect of blood pressure on structural OCT metrics and retinal perfusion in ophthalmologically healthy subjects, *Invest. Ophthalmol. Vis. Sci.*, **62** (2021), 5. https://doi.org/10.1101/2021.01.14.21249808

44. H. Alashwal, M. El Halaby, J. J. Crouse, A. Abdalla, A. Moustafa, The application of unsupervised clustering methods to Alzheimer's disease, *Front. Comput. Neurosci.*, **13** (2019), 31. https://doi.org/10.3389/fncom.2019.00031

45. F. Topouzis, M. R. Wilson, A. Harris, P. Founti, F. Yu, E. Anastasopoulos, et al., Association of open-angle glaucoma with perfusion pressure status in the Thessaloniki Eye Study, *Am. J. Ophthalmol.*, **155** (2013), 843–851. https://doi.org/10.1016/j.ajo.2012.12.007

46. Y. Ostchega, C. D. Fryar, T. Nwankwo, D. T Nguygen, Hypertension prevalence among adults aged 18 and over: United States, 2017–2018, (2020). Available from: https://www.cdc.gov/nchs/data/databriefs/db364-h.pdf

47. J. Fang, C. Gillespie, C. Ayala, F. Loustalot, Prevalence of self-reported hypertension and antihypertensive medication use among adults aged ≥18 years – United States, 2011–2015, *MMWR Morb. Mortal Wkly. Rep.*, **67** (2018). https://doi.org/10.15585/mmwr.mm6707a4

48. A. A. Divney, S. E. Echeverria, L. E. Thorpe, C. Trinh-Shevrin, N. S. Islam, Hypertension prevalence jointly influenced by acculturation and gender in US immigrant groups, *Am. J. Hypertens.*, **32** (2019), 104–111. https://doi.org/10.1093/ajh/hpy130

49. D. Wang, M. Hatahet, Y. Wang, H. Liang, Y. Bazikian, C. L. Bray, Multivariate analysis of hypertension in general US adults based on the 2017 ACC/AHA guideline: Data from the national health and nutrition examination survey 1999 to 2016, *Blood Press*, **28** (2019), 191–198. https://doi.org/10.1080/08037051.2019.1593042

50. H. Y. Chen, S. P. Chauhan, Hypertension among women of reproductive age: Impact of 2017 American College of Cardiology/American Heart Association high blood pressure guideline, *Int. J. Cardiol. Hypertens.*, **1** (2019), 100007. https://doi.org/10.1016/j.ijchy.2019.100007

51. J. J. Mpofu, C. L. Robbins, E. Garlow, F. M. Chowdhury, E. Kuklina, Surveillance of hypertension among women of reproductive age: A review of existing data sources and opportunities for surveillance before, during, and after pregnancy, *J. Women's Health*, **30** (2021), 466–471. https://doi.org/10.1089/jwh.2020.8977

52. A. A. Abrahamowicz, J. Ebinger, S. P. Whelton, Y. Commodore-Mensah, E. Yang, Racial and ethnic disparities in hypertension: Barriers and opportunities to improve blood pressure control, *Curr. Cardiol. Rep.*, **25** (2023), 17–27. https://doi.org/10.1007/s11886-022-01826-x

53. G. M. Al Kibria, Racial/ethnic disparities in prevalence, treatment, and control of hypertension among US adults following application of the 2017 American College of Cardiology/American Heart Association guideline, *Prev. Med. Rep.*, **14** (2019), 100850. https://doi.org/10.1016/j.pmedr.2019.100850

54. R. Aggarwal, N. Chiu, R. K. Wadhera, A. E. Moran, I. Raber, C. Shen, et al., Racial/ethnic disparities in hypertension prevalence, awareness, treatment, and control in the United States, 2013 to 2018, *Hypertension*, **78** (2021), 1719–1726. https://doi.org/10.1161/hypertensionaha.121.18023

55. D. K. Hayes, S. L. Jackson, Y. Li, G. Wozniak, S. Tsipas, Y. Hong, et al., Blood pressure control among non-Hispanic Black adults is lower than non-Hispanic White adults despite similar treatment with antihypertensive medication: NHANES 2013–2018, *Am. J. Hypertens.*, **35** (2022), 514–525. https://doi.org/10.1093/ajh/hpac011

56. F. Galassi, A. Sodi, F. Ucci, G. Renieri, B. Pieri, M. Baccini, Ocular hemodynamics and glaucoma prognosis: A color Doppler imaging study, *Arch. Ophthalmol.*, **121** (2003), 1711–1715. https://doi.org/10.1001/archopht.121.12.1711

57. L. Carichino, A. Harris, S. Lapin, G. Guidoboni, S. Cassani, A. De Silvestri, et al., Waveform parameters of retrobulbar vessels in glaucoma patients with different demographics and disease severity, *Eur. J. Ophthalmol.*, **30** (2020), 1019–1027. https://doi.org/10.1177/1120672119848259

58. F. Agnesi, L. Carlucci, G. Burjanadze, F. Bernini, K. Gabisonia, J. W. Osborn, et al., Complex hemodynamic responses to trans-vascular electrical stimulation of the renal nerve in anesthetized pigs, *IEEE Open J. Eng. Med. Biol.*, **5** (2024), 750–758. https://doi.org/10.1109/OJEMB.2024.3429294

59. M. Zang, P. Mukund, B. Forsyth, A. F. Laine, K. A. Thakoor, Predicting clinician fixations on glaucoma OCT reports via CNN-based saliency prediction methods, *IEEE Open J. Eng. Med. Biol.*, **5** (2024), 191–197. https://doi.org/10.1109/OJEMB.2024.3367492

60. A. Thakur, M. Goldbaum, S. Yousefi, Convex representations using deep archetypal analysis for predicting glaucoma, *IEEE J. Transl. Eng. Health Med.*, **8** (2020), 1–7. https://doi.org/10.1109/jtehm.2020.2982150

61. K. Zhou, S. Yang, Fuzzifier selection in fuzzy c-means from cluster size distribution perspective, *Informatica*, **30** (2019), 613–628. https://doi.org/10.15388/informatica.2019.221

62. M. Joyce, J. Keller, G. Guidoboni, R. Rai, B. A. Siesky, A. Verticchio, et al., Transferring clusters of glaucoma cases across studies to demonstrate the significance of selectiveness in machine learning methods. *Invest. Ophthalmol. Vis. Sci.*, **65**, (2024) 1629–1629. Available from: https://iovs.arvojournals.org/article.aspx?articleid=2795782

AIMS Press